THE ASTROPHYSICAL JOURNAL, 507:945–954, 1998 November 10

A MULTIWAVELENGTH CAMPAIGN ON γ CASSIOPEIAE. II. THE CASE FOR COROTATING, CIRCUMSTELLAR CLOUDS

MYRON A. SMITH,[1] RICHARD D. ROBINSON,[2] AND ARTIE P. HATZES[3]
Received 1998 January 5; accepted 1998 June 17

ABSTRACT

Simultaneous X-ray/UV observations over a full day on 1996 March 14–15 have been made of the prototypical B0.5e star γ Cas using the *Rossi X-Ray Timing Explorer* satellite and the Goddard High Resolution Spectrograph (GHRS) on board the *Hubble Space Telescope*. The GHRS spectra, taken in the region of the Si IV $\lambda\lambda$1394–1403 doublet, also permitted the construction of an extremely precise light curve from a nearby "pseudocontinuum" region. The continuum UV and X-ray light curves reveal a pair of X-ray maxima $\sim$10 hr apart that coincide in time with UV continuum flux "dips" of $\sim$1%. In the first paper in this series we attributed the long-term X-ray variations to magnetic activity sites on the surface of the star that undergo rotational modulation on a $\sim$1.125 days period. In the current study we find that flux and color curves generated from a 33 hr sequence of *International Ultraviolet Explorer* (*IUE*) echellegrams obtained in 1996 January display dip features similar to those in the GHRS data. Comparing the timings of the continuum flux dips and the Si IV line strength variations in both the GHRS and *IUE* data sets gives a slightly revised period of 1.123 days for both the UV and X-ray activities. This strengthens the argument that high-energy activity on γ Cas is modulated by rotation of long-lived structures close to its surface. Analysis of the pseudocontinuum light curves constructed from the GHRS and *IUE* light curves shows at least two surprising characteristics for the flux dips: (1) the dips last only $\sim$0.3 cycles, which is too brief for rotation modulation of surface features, and (2) their amplitudes increase from long to short wavelengths, which attain a maximum near 1206 Å. The character of the variations of the photospheric Si IV line profiles is unexpected in that the equivalent width fluctuations do not correlate with the slow undulations of the continuum flux. Moreover, the profile variations do not show an expected blue-to-red migration of microfeatures. We show that the continuum characteristics and absence of migration of features in the Si IV lines can be explained by the presence of very cool, optically thin clouds that corotate with the star. Assuming a tilt of the rotational axis of $+45°$ to the observer's line of sight, our model simulations of the two major dips in the UV light curves indicate that the clouds have radii of a few tenths of a stellar radius and are attached to points on the surface at low to mid-latitudes on the near hemisphere. These findings support the conclusion of the first paper in this series that γ Cas is a member of a small group of OB stars that have magnetospheres associated with X-ray activity.

Subject headings: circumstellar matter — stars: activity — stars: emission-line, Be — stars: individual (γ Cassiopeiae) — stars: rotation

1. INTRODUCTION

For over a century the prototypical "classical" Be star γ Cas has perplexed observers and frustrated theorists, exhibiting an array of activities over a large range of timescales and wavelengths. These activities include a rapidly fluctuating X-ray flux curve (see, e.g., Parmar et al. 1993), "submigrating features" in the optical lines (Yang, Ninkov, & Walker 1988; Smith 1995), long-term variations in the violet/red emission components of its Balmer lines (Doazan 1982), and both intermediate and long-term variations at high negative velocities in its ultraviolet resonance lines (Doazan et al. 1987; Telting & Kaper 1994).

This is the second paper in a series concerning a multiwavelength campaign in which we carried out simultaneous X-ray, UV, and optical spectroscopic observations designed to construct a coherent picture of the activity on γ Cas over timescales of seconds to a day. The original intent of our program was to monitor the star over a rotation cycle simultaneously in all these wavelengths. A last-minute postponement of the launch of a key instrument, the *Rossi X-Ray Timing Explorer* (*RXTE*) satellite, forced us to split the program into two monitoring efforts. The first part of our effort was a campaign with the *International Ultraviolet Explorer* (*IUE*) in high dispersion over a 33 hr interval on 1996 January 18–19. This program was undertaken in conjunction with optical spectroscopy from several ground sites. The second was a simultaneous campaign on 1996 March 14–15 using the Proportional Counter Array of *RXTE* and the Goddard High Resolution Spectrograph (GHRS) on board the *Hubble Space Telescope* (*HST*). The latter provided us with a long series of high time-resolution spectra in the region near the Si IV $\lambda\lambda$1394–1403 resonance doublet.

In Paper I of this series (Smith, Robinson, & Corbet 1998) we presented a discussion of the X-ray characteristics of γ Cas as observed with *RXTE*. In this study we found that the X-ray emission was comprised of two basic components. The first consisted of numerous, short-lived "shots" with lifetimes ranging from a few seconds to several minutes and intensities that could reach several times the background level. The second component was the background, dubbed the "basal" component, which varied in strength by as

[1] STScI/CSC, Space Telescope Science Institute, 3700 San Martin Drive, Baltimore, MD 21218; msmith@stsci.edu.
[2] Catholic University of America; and LASP, Goddard Space Flight Center.
[3] Department of Astronomy, University of Texas at Austin.

much as 40% over a period of hours. The pattern of variations in the basal X-ray flux appears to be related to the rotational period of the star (about 1.125 days) and is relatively long-lived, in that it is seen in shorter time sequences obtained by the *ASCA* satellite 11 days before our March *RXTE* observations, as well as in an *RXTE* data set that we obtained 6 months later.

In Paper I we compared these long-term X-ray variations with fluctuations in the UV continuum near 1400 Å obtained from the GHRS observations. This comparison showed a very strong anticorrelation between the UV continuum intensity and the X-ray flux, which suggests that the X-ray emission was closely associated with the source of UV continuum variability. This association, along with the rotational timescale of the variations, provided strong evidence that the X-rays were generated near the surface of the B star rather than in the accretion disk of a hypothetical degenerate companion, which had been postulated in previous studies (see, e.g., White et al. 1982; Murakami et al. 1986; Parmar et al. 1993). The analysis presented in Paper I suggests that the X-ray shots mark the occurrence of explosive, flare-like events that are generated by magnetic instabilities in a localized magnetic complex tied to the surface of the star. While some of the energy released by these events is radiated during the shot event, most of the hot (10^8 K) plasma produced will expand into an overlying magnetic canopy and contributes to the long-term basal emission. The variation in the X-ray emission results from the rotational modulation of these activity complexes across the stellar disk. How, then, do the UV continuum variations fit into this overall picture of the X-ray source?

In this paper we examine both the GHRS and *IUE* observations with the aim of understanding the source of the UV continuum variations. In § 2 we discuss the data reduction, which includes the removal of various instrumental effects. The general character of the UV observations, both in the continuum and in the Si IV lines, are then discussed in § 3. In § 4 we examine the evidence in favor of or against the two basic models: (1) starspots and (2) corotating clouds of absorbing plasma. The evidence suggests that the corotating clouds are the most probable source of the continuum variations, so we proceed to estimate the characteristics of these features, including their temperature, size, height, and average density. The conclusions are then given in § 5.

2. ULTRAVIOLET OBSERVATIONS

2.1. *GHRS Data*

The GHRS observations used the medium-resolution G160M grating and covered 36 Å centered on the Si IV $\lambda\lambda$1394–1403 resonance doublet with a spectral resolution ($\lambda/\Delta\lambda$) of 10,000. To ensure accurate photometry we observed the star through the 2″ Large Science Aperture. In addition, because we were searching for dynamic phenomena, we maximized the time resolution by using the RAPID readout observing mode with 1 s integration times. In this observing mode, spectra are integrated for the specified time without substepping and are then transmitted directly to the onboard tape recorder. This allows time sequences to be obtained with essentially no dead time between exposures. The brightness of this star resulted in spectra with 8100 counts diode^{-1} in the continuum during each 1 s integration.

Because of the high declination of γ Cas, we were able to arrange observations while the star was in the *HST* continuous viewing zone. The *HST* project assigned a total of 14 orbits to this program, each 96 minutes in length. The observations started at 21:18 UT on 1996 March 14. The first orbit was dedicated to target acquisition and various calibration exposures. The next eight orbits consisted of 91 minutes each of continuous monitoring separated by gaps of approximately 5 minutes during which a wavelength calibration exposure was obtained and the instrument performed various internal calibrations. During the final five orbits the spacecraft transited the South Atlantic Anomaly (SAA) during part of the orbit, so the on-target time was reduced to values as low as 60 minutes per orbit. Altogether, the star was monitored for 1045 minutes out of a 1280 minute total timeline.

During the analysis the observations were corrected for several instrumental effects, including fixed-pattern noise, wavelength shifts caused by the orbital motion of the spacecraft, and wavelength shifts and intensity variations resulting from the interactions of the detectors with the geomagnetic field of the Earth. This latter effect is often referred to as geomagnetically induced pertubations, or GIMPs. The fixed-pattern noise resulted from small differences in the gains of individual diodes and was removed using a high-frequency Fourier filter. The wavelength shifts were identified by cross-correlating the core of the Si IV λ1403 line with the same wavelength region in the first spectrum in the time sequence. These shifts were dominated by the GIMP effect and had an approximately sinusoidal variation with a peak amplitude of $\sim$0.5 diode widths (0.035 Å) and a period of half of the *HST* orbital period. Some residual effects of incomplete fixed-pattern noise correction can still be seen in individual flux extractions, for example, in the line profiles, but they are negligible in the integrated pseudocontinuum flux curves discussed below.

The most difficult effect to correct was the intensity variations caused by the GIMP. The size of the Large Science Aperture is designed to match the height of the diodes in the GHRS digicon detectors. When the focusing fields in the detectors interact with the geomagnetic field they cause the image of the spectrum to drift perpendicular to the axis of the diode array, so that light from the edge of the aperture falls off the diodes. This results in a slight reduction of detected flux. The problem is enhanced by the fact that the axis of the diode array is not exactly perpendicular to the dispersion direction of the spectrograph, so the intensity fluctuations become wavelength dependent, with the greatest variations occurring near the ends of the diode array. In our data set we found that the intensity varied approximately periodically, with one cycle per spacecraft orbit (96 minutes), and with a maximum amplitude variation of $\sim$0.8%. A complete description of the correction process is given in the Appendix. Because of the smoothing involved in this correction, the minimum time for believable small-amplitude continuum variations from the star is 30–45 minutes. Figure 1 shows the postprocessed, mean spectrum from these data over all observing times.

Each point in our final continuum light curve consists of binned information of some 144 pixels and 60 s. With 8100 counts s^{-1} in the continuum, the theoretical noise-to-signal ratio is 1.2×10^{-4}. A Fourier analysis of the light curve shows that the value realized is twice as large as this. Much of the excess noise occurs in the form of a 1/*f*-like "signal."

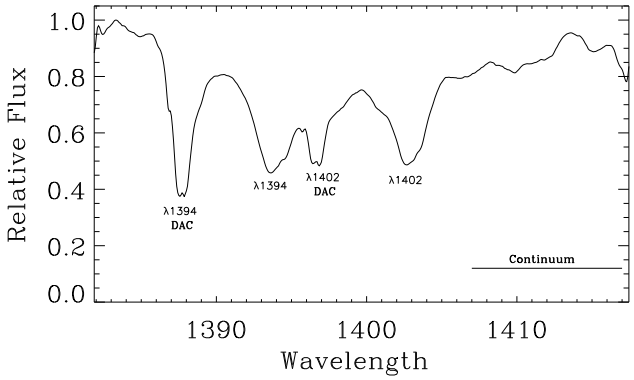

FIG. 1.—Time-averaged GHRS spectrum in the region of the Si IV $\lambda\lambda$1394–1403 doublet for γ Cas.

This signature begins at 10 minutes and rises to 3 times the high-frequency noise level at a Fourier frequency corresponding to 90 minutes (one satellite orbit). This signal could be real in the star or it could arise from errors accrued in our GIMP-filtering procedure. A detailed light curve was shown in Paper I and is also exhibited in Figure 8 below.

2.2. *IUE Data*

Our *IUE* program was designated as a Key Project for the ninteenth and final episode of the *IUE* satellite mission. Our observations consisted of 32 high-dispersion, short-wavelength echellegram images taken roughly continuously from 13:57 UT on 1996 January 18 to 22:51 UT on 1996 January 19. The image sequence numbers are SWP 56590–56621. The resolution of these data is about 0.05 Å. These spectra were reduced with a prototype version of the NEWSIPS reduction software (Nichols & Linsky 1996), which for practical purposes is identical to the version adopted to produce the final *IUE* archive.

The errors from measurements of both continuum and line fluxes of a large ensemble of the high-dispersion SWP echellegrams of γ Cas, processed through the older IUESIPS software, have been displayed and discussed by Telting & Kaper (1994). These data indicate an rms error of 4% both for equivalent widths of strong lines and for the repeatability of continuum fluxes. Although several error sources affecting *IUE* data do not have a Gaussian distribution, most of these may be neglected for rapid time-sampled observations. The NEWSIPS-processed data that we use have smaller errors that can be more reliably estimated. As a rule of thumb, the signal-to-noise ratio (S/N) per spectral resolution element can be increased for co-additions of up through seven like spectra processed through NEWSIPS, whereas such co-additions are effective in improving IUESIPS data for only three images (Nichols & Linsky 1996). A comparison of line profiles of images processed through both systems shows that the S/N in equivalent widths of strong lines is improved fully by a factor of 2 in the NEWSIPS systems (Smith 1994; Nichols & Linsky 1996).

Because we were interested only in *variations* of the line and continuum, we were able to exploit differential techniques to obtain the highest feasible S/N from the data. Therefore, we used net fluxes in order to avoid exaggerated errors at the ends of the echelle orders from the ripple correction step. In addition, we measured line strengths simply by ratioing the flux under a line to the entire flux within the order. For strong lines of Si II, Si III, C IV, and He II, we typically determined repeatability errors of 3%–4% with a conventional technique of estimating a local continuum over the line. We were able to reduce these errors signifi-

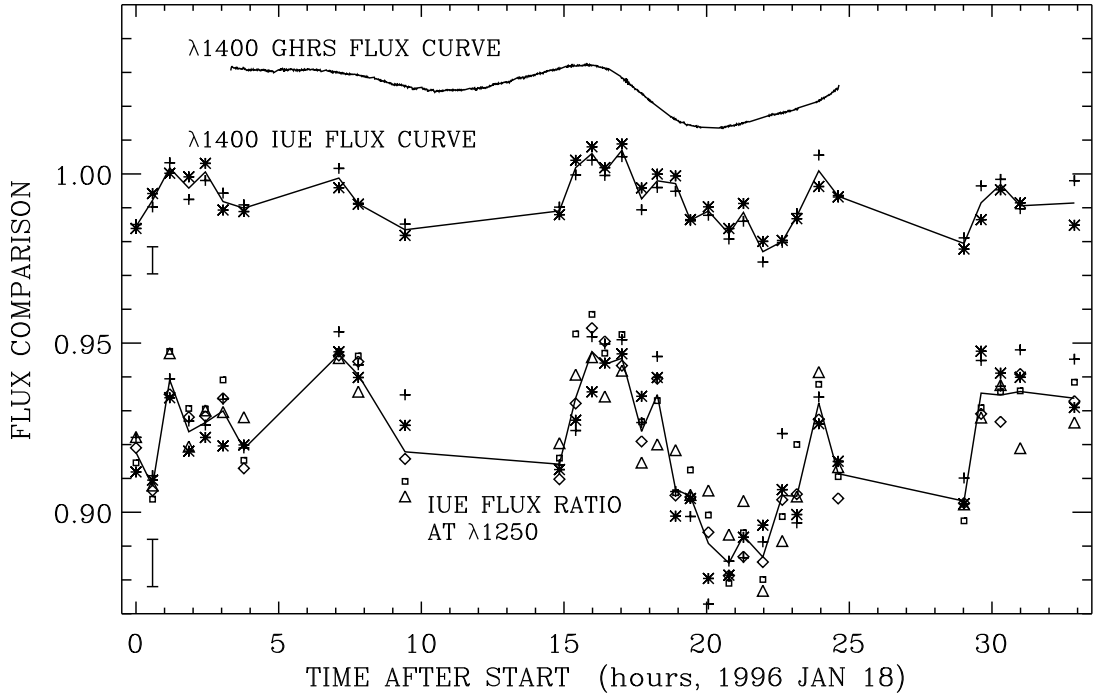

FIG. 2.—Time history of the integrated UV flux within the pseudocontinuum region between 1407 and 1411 Å in the GHRS time series. The data points represent 1 minute averages. Also shown are the integrated *IUE* fluxes for echelle orders near 1400 (*middle*) and 1250 Å (*bottom*). The intensity from several adjacent echelle orders have been plotted in each curve. Uncertainties in the flux levels can be estimated from the scatter of these points. In this plot the time axis refers to the time from the start of the *IUE* time sequence. The GHRS time history has been placed on this timescale assuming a rotation period for the star of 1.123 days. The flux levels have been normalized and shifted to facilitate comparisons.

cantly by measuring the *ratio* of the flux within a narrow bandpass selected between wavelengths in the far wings of the lines and the integrated flux of all useful wavelengths within an order. We tabulated the errors in our measurements by determining the median absolute value of the spectrum-to-spectrum fluctuation in these flux ratios. These rms errors were 2.8% for He II λ1640, 2.3% for C IV λ1552, 2.0% for Si II λ1526, 2.6% for Si III λ1300, and 2.0% for Si IV λ1403. We have chosen median values to represent the errors because they are equivalent to the mean values for a randomly varying set of measures, yet they tend to be insensitive to the presence of occasional real variations from the star. For example, we find definite phase-correlated changes in the Si IV and C IV photospheric lines. In addition, we discovered a slow, marginally significant undulation in the He II line consistent with the rotational cycle. This feature was not correlated with any other variations discussed in this paper and accounts for the slightly larger error for this line than the others.

The practical limit for using *IUE* data for ultraviolet continuum photometry is set by the ability of the telescope operator to place the stellar image at precisely the same position repetitively within the large aperture in a time series of exposures. By summing fluxes from all available echelle orders we were able to estimate this photometric error as $\pm 0.5\%$. In the analysis given in § 3, we derive flux *ratios*. For these indices telescope fine-pointing errors then effectively cancel. The rms repeatability errors for these ratios start out at $\pm 0.4\%$ at long wavelengths and increase to $\pm 0.9\%$ at short wavelengths.

3. RESULTS

3.1. *Intensity Variations*

In Figure 2 we show the flux variations in the pseudo-continuum region between 1407 and 1411 Å in the GHRS flux time series. In deriving this curve we binned the data into effective 60 s integrations and then integrated the flux over 4 Å, which generated data points whose accuracy is limited only by the extremely small jitter of the telescope. For comparison, the figure also shows the UV fluxes measured near 1400 Å and near 1200 Å in the *IUE* data. While the noise in the *IUE* flux is much larger than for the GHRS observations, it is clear that the GHRS and *IUE* curves have a very similar shape, particularly between hours 15 and 24. This suggests that the features responsible for the variations are stable enough to have lasted at least 2 months.

The alignment of the GHRS and *IUE* curves in Figure 2 is consistent with a rotation period of 1.123 days. This is close but just significantly different from the value of 1.125 days determined from the X-ray variations studied in Paper I, and we have adopted it as the actual rotational period of the star. If one adopts a rotational aspect of $\approx 45°$ from interferometric imaging of the circumstellar disk of the star in Hα (Quirrenbach et al. 1997; Stee et al. 1998), and a value of 320 km s^{-1} for $v \sin i$ (Smith 1995; see also the discussion on data preconditioning in § 4.1), this rotational period leads to a stellar radius of 10 $R_{\odot}$. This value is consistent with a somewhat evolved main sequence B0.5 star, as inferred from its parallax of 190 pc determined by the *Hipparcos* satellite (Perryman 1997).

3.2. *UV Color Variations*

The broad wavelength coverage of the *IUE* data allows us to examine possible changes in the shape of the UV continuum that might be associated with the intensity variations. To do this we took the 52 orders in each of the 32 *IUE* echelle exposures, divided them into groups of four, and then summed the unflagged fluxes in each of these groups. This procedure gave an average flux at each of 13

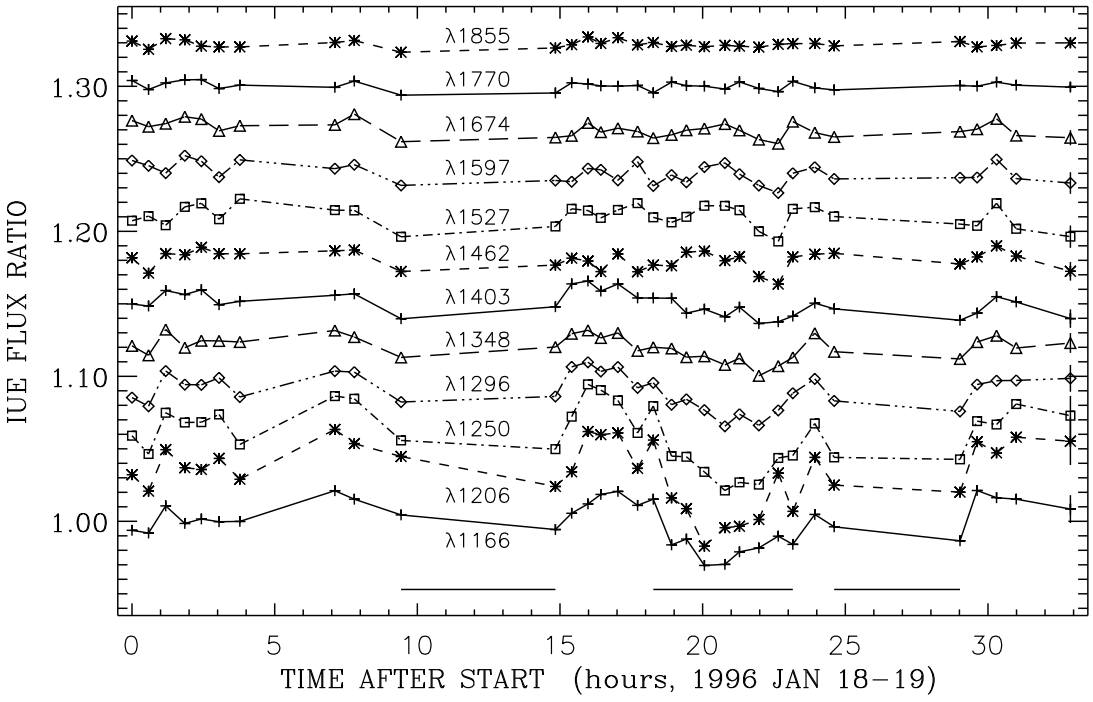

FIG. 3.—Ratios of the integrated flux over sets of four adjacent *IUE* echelle orders centered at the specified wavelengths to the integrated flux measured near λ1960 (see § 3.2.). Each curve has been normalized to its average value and shifted to facilitate comparisons. The rms values shown around the last data point were computed from means of the fluctuations of the color time histories.

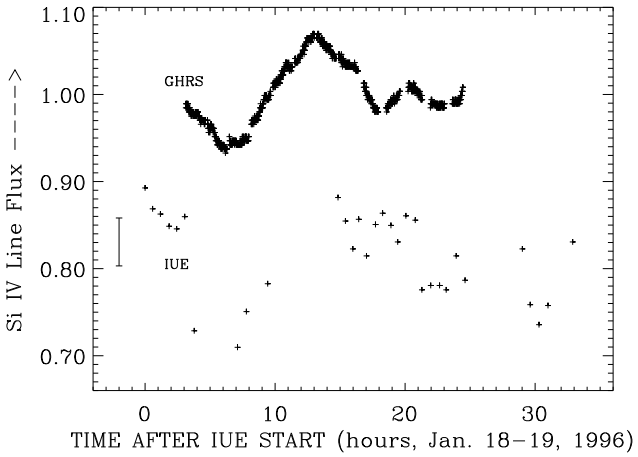

FIG. 4.—Normalized equivalent widths of the Si IV λ1403 line measured in the GHRS observations (*top*) and the *IUE* data (*bottom*). The timescale is the same as that used in Figs. 2 and 3, and the *IUE* values have been shifted downward for clarity. The average equivalent width of this line for the *IUE* epoch is 1.47 Å.

sample regions ranging in wavelength from 1150 to 1970 Å. In Figure 3 we plotted the ratios of these fluxes to that of the longest wavelength sample centered at 1960 Å. Since we are interested in the variations, rather than the absolute flux ratios, we divided each time sequence by the average flux ratio. These ratios permit a detailed examination of the fractional changes in continuum flux at each wavelength. The error bars in Figure 3 are taken from the average point-to-point fluctuations in time. The flux ratios clearly show real changes with time, with the largest variations appearing at wavelengths less than 1300 Å. Comparing these 12 curves with the flux variations (Fig. 2) shows a reddening of the spectrum during times of UV flux decrease. This behavior might be expected if the region responsible for the variations has a cooler temperature than the photosphere of the star.

3.3. Si IV *Line Variations*

The Si IV lines at 1393.7 and 1402.7 Å show two types of variability. The first is represented by strong absorption features that appear at ~ -150 km s^{-1} from line center and then drift to velocities as high as -1800 km s^{-1}. These

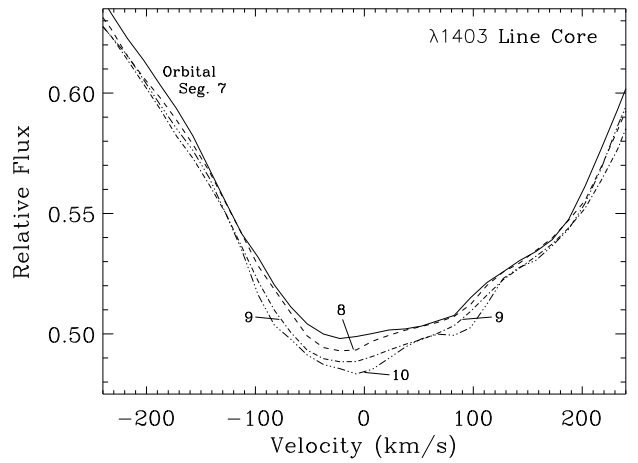

FIG. 5.—Comparison of the core region of the Si IV λ1403 profile during 10 minute segments at the end of orbits 7–10, i.e., near hours 18, 20, 22, and 24 in Fig. 2. The temporal continuum variations have been removed.

are caused by either ionization variations or density enhancements within the stellar wind and are generally referred to as discrete absorption components, or DACs. The second variation occurs within the line core of the putative photospheric component and is typically much smaller than the variations within the DACs. The variations within the high- and low-velocity components of the Si IV lines will be discussed in the third paper in this series. Here we will simply describe the properties that are most closely related to an interpretation of the variations in the UV continuum.

In Figure 4 we plot the equivalent widths of the Si IV λ1402.3 line for both the GHRS and *IUE* data sets. Because the DAC features contaminated the blue wind of the line, only that portion of the profile between -50 and 250 km s^{-1} was used in determining the equivalent width for the GHRS data. The entire profile was used for the *IUE* data because of the lower S/N there. Although the *IUE* observations again show a much higher noise level, there is a clear similarity in the EW time histories, especially during the pronounced dip centered near hour 6. Thus, the equivalent width appears to vary periodically with an ephemeris that is the same as that shown by the UV continuum and X-ray fluxes. This implies that whatever causes the Si IV EW variations is corotating with the star. Note, however, that a comparison of Figure 4 with the UV continuum variations shown in Figure 2 shows no obvious correlations between the two time series. Thus, the variations in the UV continuum and the Si IV line probably arise from totally different regions of the stellar atmosphere.

To characterize the Si IV variations further we examined the line profiles. We were particularly interested in fine structure that drifted either from blue to red, as expected for surface spots (see, e.g., Vogt & Penrod 1983) or from red to blue, as expected from a low-velocity component of the DACs. A sample comparison is shown in Figure 5. While some fine structure did appear (e.g., the narrow feature seen in orbit 10 near 100 km s^{-1}), there was no evidence for a drift in wavelength. In most cases, the profile variations were relatively broad band (covering a velocity range of 300–400 km s^{-1}) and tended to be symmetric with about 0 velocity, with the greatest intensity variations occurring at line center.

4. INTERPRETATION

There are two possible models that might explain periodic continuum variations having the rotation period of the star. The first involves large-scale temperature inhomogeneities on the stellar surface (see, e.g., Bohlender 1994), while the second assumes absorbing clouds of gas that are tied to the stellar surface by magnetic fields and are forced to corotate with the star (see, e.g., Short & Bolton 1994). In this section we will examine the evidence for each of these interpretations.

4.1. *Starspots*

To simulate the effects of starspots we developed a computer program in which the assumed intensity distribution across the stellar surface was held in a rectangular Mercator grid having a resolution of 0°.9 in latitude and 1°.8 in longitude. Our model ignored effects of rotationally induced oblateness, but incorporated a 45° rotational obliquity, limb darkening (after J. Lester 1997, private communication), and foreshortening. To simplify the problem, we

further assumed a two-component intensity distribution with the photosphere having an intensity of 1 and the spots having an intensity of 0. Once we specified spot distribution we could calculate the expected time variations by specifying a sequence of central longitudes and summing the intensity distribution over the visible disk for each of these in turn.

Our principal concern in this modeling was to fit the small-amplitude dip that is centered at phase 0.27 (hour 11) in Figure 2, since this lasted no longer than 8 hr, or about 0.3 cycles. We discovered that we could not generate light curves with dips shorter than ~ 0.42 cycles, even with drastic ad hoc assumptions for the limb darkening law and the spot latitude. The dashed line in Figure 8 below is an example of the briefest, and still unsatisfactory, flux dips we could produce with a spot model.

As a second test of the spot model we estimated the effects that such a spot would have on the Si IV line profiles to see whether these would be observable in our data. We employed the same basic computer model as that used to examine the continuum variations, except that in this case the radial velocities at each element of the surface were computed and used to shift the spectra during the integration. The photosphere was assumed to have a Kurucz (1993) spectrum consistent with $T_{\rm eff} = 28{,}000$ K and $\log(g) = 4$, while the spots had a similar spectrum calculated for $T_{\rm eff} = 20{,}000$ K and $\log(g) = 4$. We assumed that the spot was located at a latitude of 45° so it transits the projected center of the star. The area was adjusted such that the intensity was decreased by a maximum of 3%. Figure 6 shows the expected effects when the spot is at disk center and at longitudes that are plus and minus 45° from disk center. In this figure we have divided the spectra obtained when a spot is present by a reference spectrum calculated from an immaculate star. The signature of the spot is clearly evident as narrow apparent emission features for both of the Si IV lines as well as for numerous weaker lines throughout the spectrum. There is also an appreciable drift from blue to red wavelengths as the spot is advected across the surface. Note that the expected Si IV related emission features become asymmetric when the spot is away from disk center. This is caused by the large intrinsic width of the photospheric line profile.

As a final test of the starspot model, we applied the maximum entropy method (MEM) algorithm of Vogt, Penrod, & Hatzes (1987) to the variations of the photospheric component of the λ1403 line. Some preconditioning of the data was done for this step. Thus, a continuum level was first determined by fitting rotational profiles to this component until a minimization of the errors with this fit were obtained (this led to a value of 320 km s^{-1}). We also spliced the blue wing of the λ1394 line to the λ1403 profile for this modeling. We then synthesized rotationally broadened profiles as a function of rotational phase for a variety of inhomogeneous abundance-patch models, with models oriented both equator-on and at 45° to the observer. None of these models produced convincing surface maps. For example, a model that permits the local surface abundance of silicon to vary both by positive and negative values around the solar abundance fitted the profiles well, but it resulted in a sandwich-layered picture of Si-rich and Si-poor structures. Models in which the surface abundance was allowed to increase, as is observed in He-rich Bp stars, produced long, diagonally oriented features on the surface.

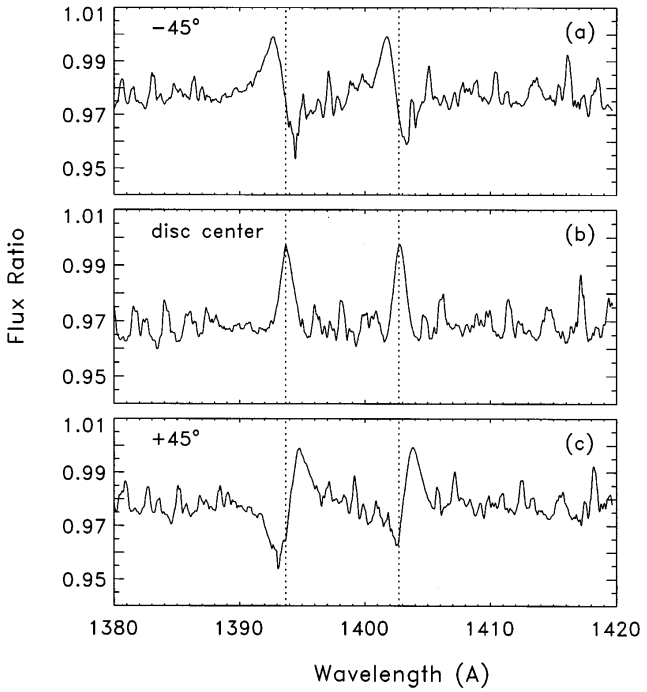

FIG. 6.—Spectroscopic fine structure in the observed GHRS wavelength region that is predicted to result from a surface spot at longitudes of (*a*) −45°, (*b*) 0° (*disk center*), and (*c*) +45° from a model of a rotating γ Cas. The spot temperature is assumed to be 24,000 K and to have an area sufficient to reduce the continuum level by a maximum of 2%. The plots represent the ratio of fluxes with the spot to those from an immaculate star disk. The vertical lines show the centers of the photospheric Si IV lines. Each of the absorption/emission features above a level of 0.2% is due to nearby weak spectral lines.

These solutions did not fit the observed line profiles well. We are convinced that the sandwich- and elongated-shaped patterns in our surface disk solutions are the MEM algorithm's attempt to compensate for the lack of blue-to-red migrating features in the line profiles.

The absence of the expected starspot related features in the observed Si IV profiles (see §3.3.), as well as the failure of a starspot model to reproduce the observed continuum variations, leads us to discard the starspot hypothesis. We now examine the alternative model of corotating, circumstellar clouds.

4.2. *Corotating Clouds*

4.2.1. *Fitting the Continuum Variations*

Continuum light-curve dips may be made arbitrarily short if they arise from absorption within an elevated cloud that is attached to the surface and forced to corotate with the star. Such entities have been described as "spokes" in the Be star literature (see, e.g., Vogt & Penrod 1983; Harmanec 1987; Short & Bolton 1994) and as "magnetospheres" in the context of Bp stars (see, e.g., Shore & Brown 1990). To evaluate this concept, we wrote an additional computer program that models the projected stellar disk as a circle on a square grid and computes the projected path of a spherical, corotating cloud against the background star disk.

There are a large number of free parameters in this modeling process, including the cloud shape, size (radius), elevation, optical depth, and the latitude at which it is attached to the stellar surface. To make the problem more tractable,

TABLE 1

MODELED SPHERICAL CLOUD PROPERTIES

Dip Feature	Latitude (deg)	Cloud Elevation (R_*)	Cloud Radius (R_*)	Transmission
Secondary	+15–+30	0.25–0.30	0.16–0.26	0.5–0.85
Reference Latitude:	+30	0.30	0.26	0.85
Primary	+30–+60	0.36–0.35	0.33–0.32	0.75–0.85
Reference Latitude:	+30	0.35	0.32	0.80
Tertiary	+15–+75	1.9–1.5	1.0–0.94	0.95–0.98
Reference Latitude:	+30	1.7	0.69	0.98

we assumed arbitrarily that the clouds are spherical in shape with a constant density throughout, so that the transmission is maximum at cloud center and decreases toward the edge. We note in passing that a pancake-shaped cloud (slab) may also serve as a reasonable geometry if the clouds are physical similar to solar prominences. We also assume that the cloud is located radially above its attached latitude. Under these assumptions there are two primary cloud properties that affect the shape of the light curve. These are the size of the cloud and the latitude at which it is anchored. A small cloud ingresses quickly onto the stellar disk and then obscures a constant fraction of the surface, so that its effect largely mirrors the stellar-limb darkening. Larger clouds, on the other hand, take a longer time to move onto the stellar disk and also tend to average out the effects of limb darkening during disk transit. Their light curves therefore tend to have broad wings (see Fig. 7*a*). On the other hand, clouds anchored at different latitudes (Fig. 7*b*) will transit different parts of the disk. At extreme latitudes parts of the cloud may not occult the disk very much and therefore have little effect on the light curve. Additionally, the projected centers of these clouds spend little or no time transiting the stellar disk, so their sizes must be large to match an observed dip amplitude. With large sizes the light curves of extreme-latitude models show very extended wings. This attribute is not seen directly in Figure 7*b*.

As the height of a corotating cloud increases, the cloud takes a shorter time to transit the disk. Thus, for a given cloud size and latitude, the time from first to last contact can be directly related to the elevation of the cloud. Once the cloud size is determined from the shape of the light curve, the cloud transmission, which also trades off against the cloud size, can be estimated from the maximum amplitude of the variation.

Our procedure of modeling the data consisted of interactively adjusting the cloud parameters and then comparing the synthetic light curves with the observations. We were able to determine acceptable fits by using three clouds. The deduced properties of these clouds are presented in Table 1, while the synthetic light curve is shown in Figure 8. In making this fit we assumed that the continuum level seen between phases 0 and 0.1 represents that of the unspotted star, since it remains constant for nearly 3 hr. Overall, the fit is very good except for the region between phases 0.42 and 0.52, where the flux exceeds 1. Note that during this time the secondary cloud is just moving off the disk, while the primary cloud is starting to move onto the star. Thus, the excess emission may result from warm ($\sim$20,000 K) material from one or both of these complexes being viewed above the limb of the star.

There is some ambiguity in the cloud properties because of the competing effects of cloud latitude and size. Thus,

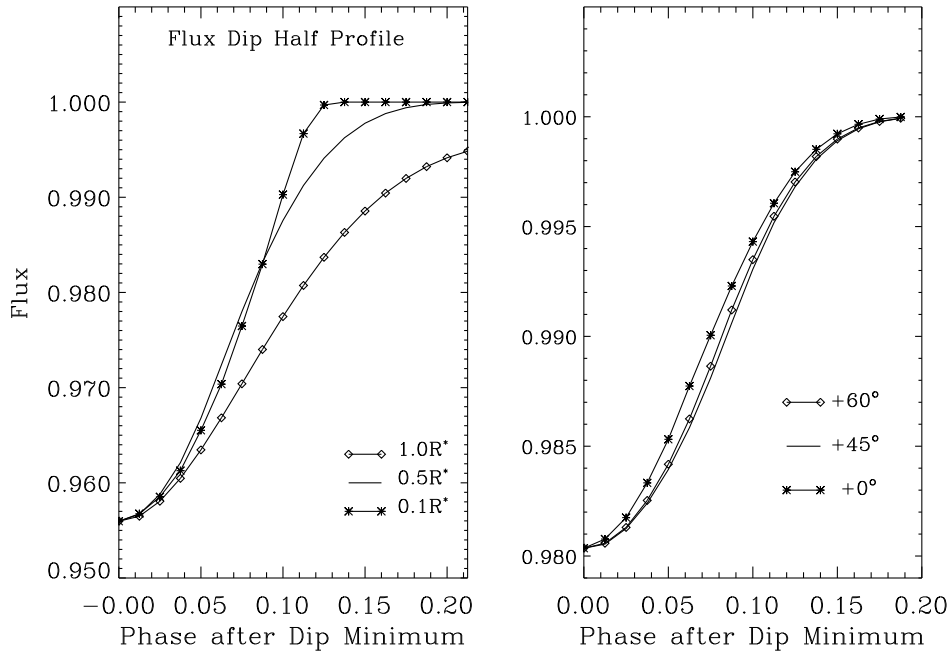

FIG. 7.—*Left:* Effect of cloud radius on the shape of the light curve resulting from the disk transit of a spherical, optically thin, corotating cloud. In all cases the clouds are assumed to be at a latitude of 30° and have an elevation of $0.3R_*$. *Right:* Effect of cloud latitude on the light curve shape. Here the elevation is $0.3R_*$, and the cloud radius is $0.3R_*$.

acceptable fits could be obtained over a range of latitudes by appropriately adjusting the size. For this reason we have presented the results in two ways in Table 1. First, since we were able to obtain acceptable fits for all of the clouds when assuming a latitude of 30°, we have tabulated the cloud size, elevation, and transmission obtained when using this latitude. Second, we tabulated the full latitude range over which acceptable fits were produced as well as the range of other parameters required in these fits. The cloud parameters given in Table 1 should be viewed only as representative numbers rather than absolute values, since they also depend upon the shape of the source. For example, if the source were a pancake (uniformly thin) slab rather than a sphere, we find that the calculated size would be about 10%–20% smaller and the transmission would be slightly larger than for the spherical model. A cloud that is elongated in the azimuthal direction will mimic a larger, less elevated, and less transparent spherical cloud. Although we have not explicitly modeled polar-elongated clouds, which are the preferred orientation of the magnetospheric tori conceived by Shore & Brown (1990) for Bp stars, we anticipate these would mimic spherical clouds that are larger, less transparent, but more elevated.

To summarize the results from Table 1, the two clouds causing the primary and secondary dips in the GHRS flux curve are likely to be attached to points on the star at intermediate latitudes and have elevations and sizes that are comparable, say $\sim 0.3R_*$. The transmissions have relatively low values of 80%–85%. The recovered light dip shown in the inset of Figure 8 must have a much higher elevation than the first two clouds, probably well in excess of a stellar radius. In order to match the ingress wing of this flux dip, both the size and transmission of the third cloud must be large. The attached latitude of this cloud is poorly constrained.

A few general inferences on the distribution of the clouds on the projected stellar surface can also be made from *IUE* results in Figure 2. The first is the suggestion of a pair of dips separated by 10 hr, which is the pattern seen more clearly in the GHRS flux curve. Second, note the hint of a dip, again accentuated at shorter wavelengths, at hours 25 and 29. This occurs at a rotational phase not included in the GHRS observations but covered by the *RXTE* observations that show a sustained maximum at this phase (Paper I). The hint of a UV continuum feature at this phase is also interesting because the *IUE* observations started at what appears to be the end of a dip. This egressing feature is consistent with the dip at hours 25–29 if indeed the rotational period is 1.123 days (27 hr). Altogether, the existence of the cloud features from the GHRS and *IUE* fluxes suggests that there may be as many as four activity complexes. Thus their arrangement is not consistent with a simple dipole geometry.

4.2.2. *Consequences from the Color Variations*

An indication of the internal properties of the clouds can be obtained from the color variations discussed in § 3. To do this we first used the SYNSPEC program (Hubeny, Lanz, & Jeffery 1994) to calculate the line-blanketed, LTE opacity as a function of wavelength for a series of isothermal clouds having a specified temperature, electron density, and turbulence. These calculations used the full Kurucz (1993) line list and assumed solar abundances. In all cases we assumed an electron density of 1×10^{11} cm^{-3} and a turbulence of 20 km s^{-1}, though the results were found to be relatively insensitive to these values. A column density was selected for each temperature so that the transmission of the cloud in the continuum near 1400 Å equaled 0.8 (see Table 1). The calculated opacities, τ_λ, were converted to transmissions, T_λ, though the relation $T_\lambda = \exp(-\tau_\lambda)$. The computed transmissions were then averaged into 20 Å wide bins over the wavelength region spanned by the SWP *IUE* camera in order to simulate the averages taken in the color analysis of the *IUE* data.

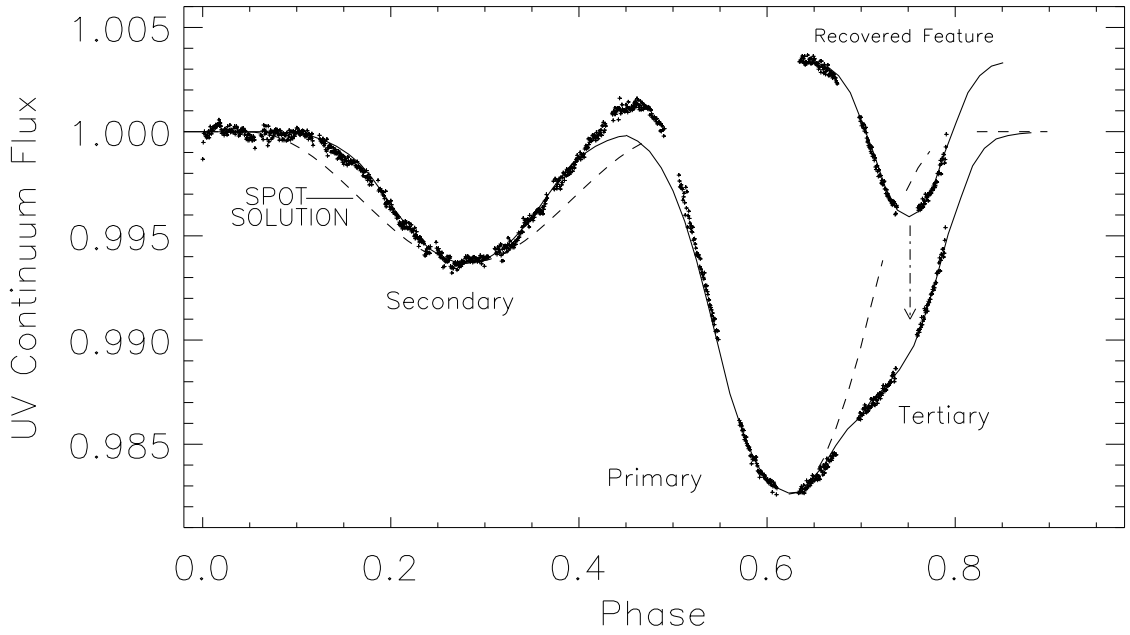

FIG. 8.—Comparison of the time history of UV continuum fluxes measured from the GHRS spectra with theoretical fits expected from clouds anchored at a latitude of 30° and having sizes, elevations, and transmissions as specified in Table 1 (*solid line*). The recovered tertiary feature and its fit are shown as an inset. The excess observed flux at phases 0.4–0.5 is interpreted as emission from hot clouds located above the stellar limb. The dotted line centered on the secondary cloud feature represents the closest fit possible with a starspot model.

If a cloud has a fractional area f given by $A_{\rm cloud}/A_{\rm star}$ and a transmission T_λ, then the observed intensity at any given wavelength $[I(\lambda)]$ will be related to the immaculate stellar intensity $[I_0(\lambda)]$ through the relation

$$I(\lambda) = I_0(\lambda)[1 - f(1 - T_\lambda)] \, . \quad (1)$$

Dividing $I(\lambda)$ by the observed intensity at a reference wavelength then gives a color index, $C(\lambda)$:

$$C(\lambda) = \frac{I(\lambda)}{I_{\rm ref}(\lambda)} = C_0(\lambda) \, \frac{1 - f(1 - T_\lambda)}{1 - f(1 - T_{\rm ref})} \, , \quad (2)$$

where $C_0(\lambda)$ is the intrinsic flux ratio for the immaculate star. Setting $C_0(\lambda)$ equal to 1, as done in Figure 3, gives an expression for the relative flux ratio variations in terms of the cloud transmission and area. Adopting a fractional cloud area of 0.1 (see Table 1), it is then possible to compare the observed color variations with those expected from different temperature clouds.

Our results for hot ($\sim$40,000 K) and warm ($\sim$20,000 K) clouds turned out not to be interesting because cloud transmissions are relatively constant. The resulting colors are almost gray, yielding transmissions of $\sim$0.99 for a column density of 10^{22} cm^{-2}. For cloud temperatures below about 15,000 K, absorption by the well-known "iron curtain" begins to dominate the continuum absorption. It is not until we reach cloud temperatures below 10,000 K that we see the drop in the flux below 1300 Å that shows up in the observations. This is a combination of line blanketing and the red wing of Lyα absorption caused by the recombination of hydrogen at these cooler temperatures.

In Figure 9 we compare the expected color changes for cloud temperatures of 9000, 7000, and 5000 K with the observed color amplitudes taken from the center of the main intensity dip (at hour 21) in Figure 3. The hydrogen column density used in these models was 1×10^{22} cm^{-2}. Although it is likely that a cloud would actually show a range of temperatures, the fits to our coolest models are reasonably satisfactory. This agreement is additional evidence that clouds, not spots, are responsible for the UV continuum variations. The cool temperature of the clouds would also naturally account for the fact that they produce no visible signature in the Si IV line profiles.

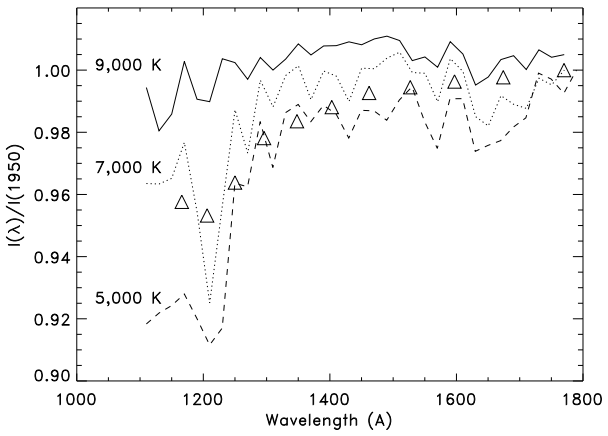

FIG. 9.—Theoretical, line-blanketed flux variations with wavelength caused by optically thin clouds with an area of 0.1 R_*, a transmission near 1400 Å of 80% (see Table 1), and temperatures of 9000, 7000, and 5000 K. The curves are normalized to 1 at a wavelength of 1960 Å. Triangles show the measured flux changes at hour 21 (Fig. 2), which is at the center of the primary UV continuum dip. Estimated errors range from the size of the symbols at short wavelengths to about half this value at long wavelengths.

5. CONCLUSIONS

A number of results have emerged from the study of the variations of the ultraviolet continuum and photospheric Si IV doublet of γ Cas:

1. The UV continuum variations observed with the GHRS can also be identified in a time series of *IUE* spectra taken 2 months earlier. This fact suggests that the regions responsible for these variations are stable over at least that time interval.

2. Phasing the *IUE* and GHRS light curves allowed us to refine the rotational period of the star. The revised period is 1.123 days.

3. The Si IV equivalent width varied on the stellar rotation period; however, variations in the Si IV lines were uncorrelated with those seen in the UV continuum, which suggests that the two effects arise from different regions. The Si IV line profile variations are complicated and our discussion regarding them is postponed to Paper III in this series.

4. The continuum variations are unlikely to originate from low-temperature regions on the stellar surface (i.e., starspots). Such features are not able to account for the relatively short lifetime of the individual dips in the UV flux curve and would also produce a well-defined spectroscopic signature in the Si IV line profile, which is not observed.

5. The most likely source of the UV variations are optically thin clouds that are forced to corotate with the star. These clouds have areas of about 10% of the stellar disk and are typically suspended from 0.2 to 0.4R_* above the surface, although there is evidence for clouds also at a much greater height (e.g., 1.7R_*). Assuming a gas density of $\sim 10^{11}$ cm^{-3}, the clouds have a typical mass of $10^{-11}\,M_\odot$ and a physical depth scale of 10^6 km. The low temperature of about 7000 K explains why these clouds do not leave a signature in the Si IV line profiles.

The close association between the UV and X-ray variations discussed in Paper I implies that the cool clouds are probably formed in the same, presumably magnetic, complexes as those producing the observed X-ray flux. The derived cool temperatures for the clouds therefore were a surprise to us, given the high levels of X-rays as well as the strong UV radiation from γ Cas itself. However, Cameron-Collier & Robinson (1989) have discussed similar cool cloud-like structures for the case of the active G8–K0 V star AB Dor. They point out that in magnetic prominence models that have low nonradiative heating rates, plasma structures will be forced to high densities and low temperatures by a thermal instability (Serio et al. 1981). The cloud densities, temperatures, and magnetic loop lengths in their models are all similar to the values we have determined for the clouds in γ Cas. Thus, a reasonable picture for producing cool corotating clouds might involve a similar thermal instability mechanism.

A loose end in our analysis is the occurrence of a brief flux maximum in the light curve, which amounts to 2.7% at phase 0.47 (Fig. 8, phase 0.4–0.5). A straightforward explanation of this feature is that it is the thermal emission from a *warm* circumstellar cloud seen beyond the limb. Indeed, if the cloud had an ambient temperature of the outer atmo-

sphere (18,000–20,000 K), one can show that this "excess emission" is consistent with the cloud sizes derived in Table 1. This conclusion is contradicted, however, by the cool cloud temperature and hence low emissivity in the ultraviolet implied by our analysis of the *IUE* color data. A conceivable way around this problem is to suppose that the clouds are larger than the values we derived for the homogeneous case and that they contain a mixture of both cool and hot temperature volumes. A suitably thermally stratified cloud could then explain all the color and monochromatic flux changes we have reported.

We are indebted to Ivan Hubeny for porting his SYNSPEC line synthesis program to our computer and for pointing out to us the spectral signature of infalling comets onto rapidly rotating stars. It is a pleasure to thank John Lester for his calculation of ultraviolet limb darkening functions for our use, and Steve Shore and Blair Savage for discussions on a number of issues addressed in this paper, particularly concerning the Lyα blanketing by an occulting cloud. This study was supported in part by NASA contract GO-6086.01-94A.

APPENDIX A

REMOVAL OF GIMP EFFECTS FROM THE GHRS DATA

Geomagnetically induced motion pertubations (or GIMPs) result from the interaction of the internal focusing fields of the GHRS detector with the geomagnetic field of the Earth. This interaction can cause the image of the spectrum to shift perpendicular to the dispersion so that parts of the spectrum fall off the detector diodes, which results in a variation in the detected intensity. The effect is particularly difficult to correct because the axis of the diode array is not exactly perpendicular to the dispersion direction, and therefore the magnitude and form of the variations varies along the array.

Our correction procedure started by reducing the number of spectra to a manageable level by binning the time sequence into effective 60 s integrations.

We then defined "windows" of about 285 km s^{-1} (19 pixels) width at 10 locations across the array, three to the blue of the various components of the λ1394 line and seven to the red of the photospheric λ1403 line. These windows are comparable to the velocity cycle length of small migrating features that appear throughout the pseudo-continuum region of the spectrum (Smith 1995). When all fluxes within a window are binned together, the positive and negative excursions of the migrating pattern tend to average out. We then constructed time histories of the total fluxes within each of these windows. Each of these 10 flux histories showed a sinusoidal-dip pattern, which is the GIMP distortion to be removed. Our next step was to fit the maxima of each sinusoidal time history with a ninth-degree Chebyshev polynomial. This particular function is sensitive to the curvature in the actual variable flux output from the star late in our observations, yet it did not cause artificial ringing. This fitted function then represents an estimate of the actual flux of the star at the wavelength of the particular window, while the ratio of the estimated flux and the observed flux in each window represents the multiplicative correction factor to be applied at that wavelength. Next, we fitted a second-order polynomial function at each 1 minute time interval through the appropriate set of 10 correction factors, thereby specifying the correction at each wavelength point. The corrected spectrum was then determined simply by multiplying the observed spectrum by the deduced parabolic correction factor. Note that our corrections remove most or all of any stellar signal having a timescale less than $\sim$30 minutes.

Inspection of the corrected fluxes showed occasional fluctuations in a particular wavelength range compared to the fluxes in neighboring spectra. We interpreted these local fluctuations as signatures of mild ringing and therefore suppressed them by passing an FFT filter through the time histories of all 500 pixels in the spectra, rejecting any single deviations (i.e., filtering out signals shorter than 2 minutes). This final step removes any data signal, instrumental or otherwise, for timescales shorter than this limit.

REFERENCES

Bohlender, D. A. 1994, in Pulsation, Rotation, and Mass Loss in Early-Type Stars, ed. L. Balona, H. Henrichs, & J. Le Contel (Dordrecht: Kluwer), 155
Cameron-Collier, A., & Robinson, R. D. 1989, MNRAS, 236, 57
Doazan, V. 1982, in B Stars with and without Emission Lines, ed. A. Underhill & V. Doazan, NASA SP-456, 326
Doazan, V., Bourdonneau, B., Rusconi, L., Sedmak, G., & Thomas, R. N. 1987, A&A, 182, L25
Harmanec, P. 1987, in Physics of Be Stars, ed. A. Slettebak & T. P. Snow (Cambridge: Cambridge Univ. Press), 339
Hubeny, I., Lanz, T., & Jeffery, S. 1994, Newsl. on Anal. of Astron. Spectra, 20, 30
Kurucz, R. L. 1993, Kurucz CD-ROM 13 (Cambridge: Smithsonian Astrophysical Observatory)
Murakami, T., Koyama, K., Inoue, H., & Agrawal, P. C. 1986, ApJ, 310, L31
Nichols, J. S., & Linsky, J. L. 1996, AJ, 111, 517
Parmar, A., Israel, G., Stella, L., & White, N. 1993, A&A, 275, 227
Perryman, M. 1997, The *Hipparcos* and *Tycho* Catalogues, ESA SP-1200
Quirrenbach, A., et al. 1997, ApJ, 479, 477
Serio, S., Peres, G., Vaiana, G. S., Golub, L., & Rosner, R. 1981, ApJ, 243, 288
Shore, S. N., & Brown, D. N. 1990, ApJ, 365, 665
Short, I., & Bolton, C. T. 1994, Pulsation, Rotation, and Mass Loss in Early-Type Stars, ed. L. Balona, H. Henrichs, & J. Le Contel (Dordrecht: Kluwer), 173
Smith, M. A. 1994, Record of the IUE Three Agency Coordination Meeting (Noordwijk: ESA)
———. 1995, ApJ, 442, 812
Smith, M. A., Robinson, R. D., & Corbet, R. H. D. 1998, ApJ, 503, 877 (Paper I)
Stee, Ph., Vakili, F., Bonneau, D., & Mourard, D. 1998, A&A, 332, 268
Telting, J. H., & Kaper, L. 1994, A&A, 284, 515
Vogt, S. S., & Penrod, G. D. 1983, ApJ, 275, 661
Vogt, S. S., Penrod, G. D., & Hatzes, A. P. 1987, ApJ, 321, 496
White, N. E., Swank, J. H., Holt, S. S., & Parmar, A. 1982, ApJ, 263, 277
Yang, S., Ninkov, Z., & Walker, G. A. H. 1988, PASP, 100, 233